Quantifying supraglacial debris-related melt-altering effects on the Djankuat Glacier, Russian Federation, Part 1: comparison of surface energy and mass fluxes over clean and debris-covered ice

Yoni Verhaegen[1], Oleg Rybak[1,2,3], Victor V. Popovnin[4], and Philippe Huybrechts[1]

[1]*Departement Geografie, Vrije Universiteit Brussel, Pleinlaan 2, 1050 Brussels, Belgium*
[2]*Water Problems Institute, Russian Academy of Sciences, Gubkina Str. 3, 119333 Moscow, Russia*
[3]*Kabardino-Balkarian State University, Chernyshevskogo Str. 173, 360004, Nalchik, Russia*
[4]*Department of Geography, Lomonosov Moscow State University, 1 Leninskiye Gory, 119991 Moscow, Russia*

Corresponding author: Yoni Verhaegen (yoni.verhaegen@vub.be) (ORCHID ID 0000-0002-0164-2086)

Key Points:

- We investigate the differences between the energy and mass fluxes over clean ice and debris-covered ice surfaces of the Djankuat Glacier.
- The glacier surface-atmosphere interaction over debris-covered ice is found to be significantly modified if compared to clean ice surfaces.
- The eventual effect of the supraglacial debris on the energy and mass fluxes highly depends on the debris-covered area and debris thickness.

Key Words:

- glacier
- debris cover
- ice
- meteorology
- numerical modelling

Abstract

This work presents a comparison of the meteorology and the surface energy and mass fluxes of the clean ice and debris-covered ice surfaces of the Djankuat Glacier, a partly debris-covered valley glacier situated in the Caucasus. A 2D spatially distributed and physically-based energy and mass balance model at high spatial and temporal resolution is used, driven by meteorological data from two automatic weather stations and ERA5-Land reanalysis data. Our model is the first that attempts to assesses the spatial variability of meteorological variables, energy fluxes, mass fluxes, and the melt-altering effects of supraglacial debris over the entire surface of a (partly) debris-covered glacier during one complete measurement year. The results show that the meteorological variables and the surface energy and mass balance components are significantly modified due to the supraglacial debris. As such, changing surface characteristics and different surface temperature/moisture and near-surface wind regimes persist over debris-covered ice, consequently altering the pattern of the energy and mass fluxes when compared to clean ice areas. The eventual effect of the supraglacial debris on the energy and mass balance and the surface-atmosphere interaction is found to highly depend upon the debris thickness and area: for thin and patchy debris, sub-debris ice melt is enhanced when compared to clean ice, whereas for thicker and continuous debris, the melt is increasingly suppressed. Our results highlight the importance of the effect of supraglacial debris on glacier-atmosphere interactions and the corresponding implications for the changing melting patterns and the climate change response of (partly) debris-covered glaciers.

Plain Language Summary

The presence of a cover of rocks and sediments can significantly modify the melting patterns and climate change response of mountain glaciers. In the Caucasus region, a significant amount of glacier surfaces has been (partly) covered with such supraglacial debris, including that of the Djankuat Glacier, a well-studied glacier at the border of Georgia and the Russian Federation. This study investigates how the presence of debris changes the surface-atmosphere interaction of the glacier in terms of its energy fluxes, mass fluxes and ice melt production. We use meteorological input from two on-glacier automatic weather stations and extend these data over the entire glacier surface to directly compare the surface conditions over both the clean ice and debris-covered ice surfaces of the gglacier. Our results show that the energy and mass balance at the glacier surface are significantly modified due to the debris, resulting in different melting regimes over both surface types. The degree of melt modification is found to highly depend on the debris-covered area and debris thickness: for thin/patchy debris, melt rates can be slightly enhanced when compared to clean ice surfaces, whereas for thick and continuous debris, the melting of ice is increasingly suppressed due to shielding effects.

1 Introduction

In a warming climate, debris cover on mountain glaciers is believed to increase drastically, due to the build-up of more englacial melt-out material, lower ice flow velocities, and an increased slope instability (e.g. Kirkbride, 2000; Jouvet et al., 2011; Carenzo et al., 2016). In the context of the current warming climate (e.g. Masson-Delmotte et al., 2021), a sharp increase of debris-covered glacier surfaces has therefore already been observed worldwide during the last decades, but was especially noted in the Caucasus (e.g. Stokes et al., 2007; Popovnin et al., 2015; Scherler et al., 2018). Consequently, supraglacial debris cover has expanded at a rate of $+0.23\ \%\ \mathrm{yr}^{-1}$ between 1986 and 2014 when considering the entire Caucasus region (Tielidze et al., 2020).

Evidently, the presence of supraglacial debris can significantly influence the melting patterns of mountain glaciers, of which the eventual effects depend on the debris area and thickness, its physical and geometrical properties, and the local climatic conditions (e.g. Østrem, 1959; Reid and Brock, 2010; Miles et al., 2022). All of the aforementioned factors directly affect the net energy flux at the glacier surface and in that way determine the extent of momentum, heat and moisture exchange between the atmosphere and the surface (e.g. Huo et al., 2021; Winter-Billington, 2022). A better understanding of these processes is crucial in determining the behavior and climate change response of clean ice and (partly) debris-covered mountain glaciers. Although a comparison of the energy and mass fluxes over clean ice and debris-covered ice surfaces is still scarce in the literature, previous research has shown that the surface energy and mass balance differ notably when both surface types are compared to one another (e.g. Yang et al., 2017; Potter et al. 2020; Nicholson and Stiperski, 2020; Steiner et al., 2021; Miles et al., 2022). However, none of the earlier-mentioned studies considered a direct comparison of the energy and mass balance over clean ice and debris-covered ice over the entire surface of the same glacier. This would, however, be beneficial to minimize the effects of a potentially large climatic variability over short distances in mountain regions (e.g. Hagg et al., 2010; Maussion et al., 2014), which may have interfered with the quality of regional or interglacier comparisons in earlier studies. Moreover, previous work has either (1) not included the effect of the fractional debris-covered area on sub-debris melt regimes or (2) merely used point data as a basis for their investigation (mostly the location of an automatic weather station). An upscaling of the energy and mass fluxes to perform a full 2D comparison of debris-free and (fractionally) debris-covered ice areas on the same glacier therefore remains provisionally untouched in the literature.

In our research, we focus on comparing the 2D field of the meteorological variables and the surface energy and mass balance of the clean ice and debris-covered ice of the Djankuat Glacier, a partly debris-covered World Glacier Monitory Service (WGMS) reference glacier in the Caucasus region. The main objectives are (1) to investigate the differences between spatially distributed meteorological variables and the mass and energy fluxes over clean ice and debris-covered ice surfaces of the same glacier, and (2) to quantify the influence of the debris thickness and area on the energy and mass fluxes over debris-covered ice.

2 Location, data and models

2.1 The Djankuat Glacier

The Djankuat Glacier (43°12′N, 42°46′E) is a northwest-facing and partly debris-covered temperate valley glacier situated in the Caucasus Mountain Range, near the Russian-Georgian border (Fig. 1). The glacier has been monitored extensively since the start of the annual monitoring program in 1967 CE, in which measurements relate to glacier geometry, supraglacial debris cover and the surface mass balance (e.g. Popovnin and Naruse, 2005; Popovnin et al., 2015; Rets et al., 2019; WGMS, 2022). In 1968 CE, the glacier occupied an area of ca. 2.90 km^2 and had a length of ca. 3.5 km when taken from its highest point. For 2020 CE conditions, satellite imagery revealed that the glacier area has further shrunk to ca. 2.30 km^2, while its length shortened to 3.1 km (WGMS, 2022). In accordance with the observed shrinkage, the glacier's cumulative mean surface mass balance during the 1967/68-2021/22 period exhibits a strongly negative value of −16.6 m w.e. (WGMS, 2022).

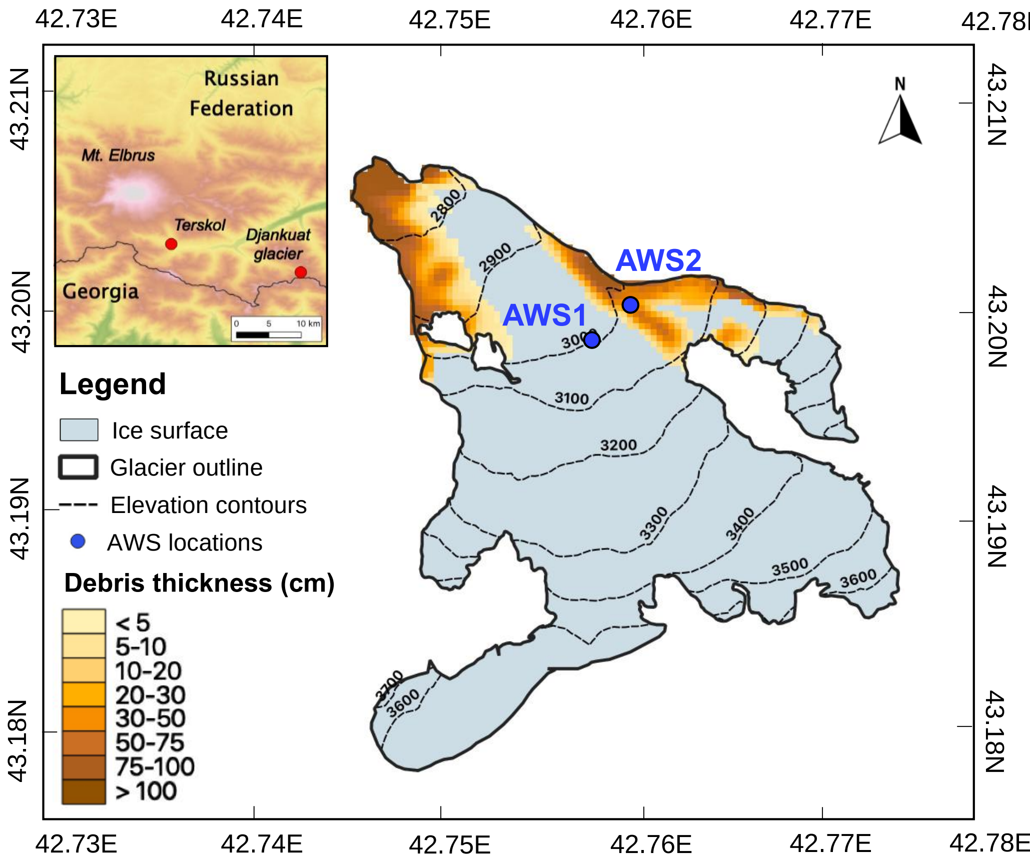

Figure 1. Sketch of the Djankuat Glacier for 2010 conditions with debris thickness map (Popovnin et al., 2015) and AWS locations (Rets et al., 2019).

2.2 Supraglacial debris cover

The surface of the Djankuat Glacier is partly covered with debris, consisting mainly of gneiss/granite-type rocks. Repeated measurements between 1968 and 2010 CE reveal that both the glacier-averaged debris thickness and the debris-covered area have increased significantly over the years (at a rate of ca. +0.010 m yr^{-1} and +0.006 km^2 yr^{-1}, correspondingly). During the 2009/2010 measurement year, the average thickness of the debris was estimated to be 0.54 m, while 13% of the glacier surface was debris-covered (Popovnin et al., 2015).

Bozhinskiy et al. (1986) investigated the properties of the debris cover on the Djankuat Glacier and reported a value for the rock thermal conductivity k_r of 2.8 ± 15% W m^{-1} K^{-1}. The same study also reports values of 2600 kg m^{-3} and 1260 J kg^{-1} K^{-1} for the density (ρ_r) and specific heat capacity (c_r) of the gneiss/granite-type rocks, and found a debris cover porosity ϕ_d of 0.43. The porosity of the debris cover on the Djankuat Glacier has furthermore been noted to decrease with depth, due to fine particles being transported downwards by air, water or gravity (Popovnin and Rozova, 2002). This process, supplemented with melt-out of fine glacial till from the ice beneath, causes finer fractions to concentrate at the bottom of the debris layer, creating an apparent vertical porosity gradient γ_{ϕ_d}).

2.3 Meteorological, reanalysis and mass balance data

As a forcing of our model, we make use of the meteorological data from two on-glacier automatic weather stations (AWSs) that were operational during the summer of 2009 (Fig. 1). AWS1 was placed on bare ice at ca. 2960 m above sea level (43.198°N, 42.757°E), and AWS2 was installed on top of debris-covered ice (fractional debris-covered area A_d/A = 1 and debris thickness h_d = 43 cm) at ca. 3025 m (43.201°N, 42.759°E). Both AWSs started fully operating on 1 July 2009 and recorded relative humidity, air temperature, shortwave and longwave radiation, wind speed and direction, and atmospheric pressure at 2 m above the ice (Rets et al., 2019). Both AWSs were also equipped with a sonic ranger sensor (located on a construction drilled into the ice) and remained operational until 30 September 2009, although AWS2 exhibited regular data gaps. As the AWS2 was removed after the summer of 2009, we select the 2008/09 measurement year as our investigation period. To supplement the AWS data records outside of their monitoring period, ERA5-Land reanalysis data were used from 1 October 2008 onwards (Muñoz-Sabater, 2019). These data were integrated into the AWSs time series by matching the mean and standard deviation of the overlapping parts of the datasets, see Table 1 (e.g. Huss and Hock, 2015).

Surface mass balance (SMB) estimates, resulting from an extensive network of ablation (by stakes) and accumulation (by snow pits) measurements that are interpolated and extrapolated to obtain a glacier-wide cover, show a value of -0.23 m yr^{-1} w.e. for the 2008/09 measurement year. The additional assumption is made that differences in debris thickness and area are negligible during the 1-year time frame between the 2008/09 (the AWS and SMB data) and 2009/10 (the debris acquisition period) measurement years.

2.4 Spatialization of meteorological data

A 25 m resolution DEM (Digital Elevation Model) from Morozova and Rybak (2017) of the glacier was the primary source to spatialize the meteorological time series from both AWSs and ERA5-Land data into a 2D field (Table 1). For air temperature T_a, the DEM was used to calculate elevation-dependent temperature gradients (γ_T) between AWS1 and AWS2 data. Air pressure p (spatialized using the barometric equation) was then used together with air temperature T_a and relative humidity RH_a (the latter was assumed to be spatially constant) to calculate the specific humidity (q_a) through the Clausius-Clapeyron equation (Table 1).

Precipitation P was not measured by the AWSs but was taken from the Terskol meteo station (at an elevation of 2141 m, approximately 20 km NW of the glacier, see Fig. 1). It was scaled using an elevation-dependent precipitation (γ_P) gradient, similar to Verhaegen et al. (2020). As precipitation patterns in the area are complex and subject to effects of orography, spatial gradients and atmospheric circulations patterns (e.g. Popovnin and Pylayeva, 2015), we chose to use γ_P as a tuning factor for the clean ice mass balance model (see section 3.1). When data gaps existed in the AWS records, air temperatures from Terskol were also used to further spatialize T_a (Table 1).

Spatially distributed wind modelling is more challenging and involves complex relationships with respect to topography and thermal/dynamic atmospheric processes (e.g. Gabbi et al., 2014; Ayala et al., 2017; Potter et al., 2020). In this study, the wind pattern is spatialized using equations from the MicroMet model (Liston and Sturm, 1998; Liston and Elder, 2006). The implementation of this method has already been done in previous snow simulations and mass balance modelling, and showed adequate results (e.g. Gascoin et al., 2013; Mernild et al., 2017; Ayala et al., 2017).

Table 1. Data sources and the corresponding spatializaton and temporalization methods of the meteorological variables used in this study. The monitoring period of both AWSs is restricted to 1 July 2009 until 30 September 2009 (including some data gaps).

	Clean ice areas			**Debris-covered ice areas**		
Data source / spatialization method	**Inside AWS monitoring period**	**Outside AWS monitoring period / gaps**	**Spatialization with DEM**	**Inside AWS monitoring period**	**Outside AWS monitoring period / gaps**	**Spatialization with DEM**
Air temperature T_a	AWS1	ERA5-Land / Terskol	Elevation-dependent temperature gradient γ_T (Terskol/AWS2)	AWS2	ERA5-Land / Terskol	Elevation-dependent temperature gradient γ_T (Terskol/AWS1)
Precipitation P	Terskol	Terskol	Elevation-dependent precipitation gradient γ_P (Terskol)	Terskol	Terskol	Elevation-dependent precipitation gradient γ_P (Terskol)
Wind speed u	AWS1	ERA5-Land	MicroMet model equations (topographically modified)	AWS2	ERA5-Land	MicroMet model equations (topographically modified)
Specific humidity q_a	AWS1 (RH_a spatially constant)	ERA5-Land	Clausius-Clapeyron equation	AWS2 (RH_a spatially constant)	ERA5-Land	Clausius-Clapeyron equation
Atmospheric transmissivity τ (for Q_S)	AWS1	ERA5-Land	Spatially constant AWS1 value / ERA5-Land value	AWS2	ERA5-Land	Spatially constant AWS2 value / ERA5-Land value
Sky emissivity ε_a (for Q_L)	AWS1	ERA5-Land	Spatially constant AWS1 / ERA5-Land value	AWS2	ERA5-Land	Spatially constant AWS2 value / ERA5-Land value

2.5 Surface mass balance model

The model used in this research is a surface mass balance model that accounts for both the clean ice and debris-covered ice araes of the Djankuat Glacier. It consists out of an accumulation (section

2.5.1) and runoff (section 2.5.2) part and is forced by several meteorological input data (sections 2.3 to 2.4 and Table 1).

2.5.1 Accumulation model

The model assumes that accumulation only depends on the occurrence of solid precipitation P_S, for which the threshold temperature for the rain-snow distinction was set to 2°C. We further assume here that accumulation is not altered by snow redistribution processes.

2.5.2 Runoff model

2.5.2.1 Surface energy balance

The starting point of the runoff model is the surface energy balance (SEB) for a snow or clean ice surface (h_d = 0) and a snow-free debris-covered glacier surface (h_d > 0 and h_s = 0):

$$\begin{cases} Q_S + Q_L + Q_{SH} + Q_{LH} + Q_R + Q_M = 0 & if\ h_d = 0 \\ Q_S + Q_L + Q_{SH} + Q_{LH} + Q_R + Q_C = 0 & if\ h_d > 0\ \&\ h_s = 0 \end{cases} \quad (1)$$

where Q_S is the net shortwave radiation, Q_L the net longwave radiation, Q_{SH} the sensible heat flux, Q_{LH} the latent heat flux, Q_M the energy flux available for melting and Q_C the conductive heat flux, which is assumed 0 for a snow/ice surface, and Q_R the heat flux by rain. At last, h_d is the debris thickness and h_s is the snow depth. Energy balance components are taken positive when directed towards the surface and all have units of W m^{-2}.

A) Net radiation flux

The net shortwave radiation is given as (with α the surface albedo and τ the sky transmissivity):

$$Q_S = S_\downarrow - S_\uparrow = S_\downarrow(1-\alpha)\tau \quad (2)$$

The downward solar radiation $S_\downarrow$ (W m^{-2}) is calculated using basic astronomical formulas (e.g. Duffie and Beckman, 2006) and also considers geometric influences on incident solar radiation, self-shading and topographic shadowing (e.g. Nemec et al., 2009). The albedo is parameterized as a function of the snow, ice and debris albedo (that are known from the AWSs), and the snow depth h_s. Here, we follow the parameterization of Oerlemans and Knap (1998):

$$\alpha = \begin{cases} \alpha_s + (\alpha_i - \alpha_s)\, exp\left(\dfrac{-h_s}{d_i^*}\right) & if\ h_d = 0 \\ \alpha_s + (\alpha_d - \alpha_s)\, exp\left(\dfrac{-h_s}{d_d^*}\right) & if\ h_d > 0 \end{cases} \quad (3)$$

where the characteristic snow depth d_i^* is taken as 0.011 m w.e. for snow/ice surfaces (e.g. Nemec et al., 2009). The characteristic snow depth for debris surfaces d_d^* increases with debris thickness until a certain thickness h_d^s:

$$d_d^* = \begin{cases} d_i^* + h_d & if\ h_d < h_d^s \\ d_i^* + h_d^s & if\ h_d \geq h_d^s \end{cases} \tag{4}$$

where h_d^s is set to 0.03 m, corresponding to the value used in the parameterization of Lejeune et al. (2013). The transmissivity τ is hereby kept spatially constant at each time step (Table 1). The net longwave radiation is the difference of incoming ($L_\downarrow$) and outgoing longwave ($L_\uparrow$) radiation:

$$Q_L = L_\downarrow - L_\uparrow = \varepsilon_a \sigma T_a^4 - \begin{cases} \varepsilon_s \sigma T_s^4 & if\ h_d = 0 \\ \varepsilon_d \sigma T_s^4 & if\ h_d > 0\ \&\ h_s = 0 \end{cases} \tag{5}$$

where σ is the Stefan-Boltzmann constant, ε_a the sky emissivity (also assumed to exhibit a spatially constant value at each time step, Table 1) and T_s the surface temperature (K). The surface emissivity was assigned a typical value of ε_s = 0.97 for snow and ice (e.g. Reid and Brock, 2010) and was put to ε_d = 0.90 for rough granite-type rocks (e.g. Harris et al., 2013).

B) Turbulent fluxes

The sensible and latent heat fluxes were calculated using the bulk aerodynamic method, following Paterson (1994) and Oerlemans (2001):

$$Q_{SH} = c_a \rho_a C_E u \Delta T \tag{6}$$
$$Q_{LH} = L_v \rho_a C_E u \Delta q \tag{7}$$

where c_a is the specific heat capacity of air, u the wind speed, L_v the latent heat of vaporization of water, ρ_a the air density, C_E is a dimensionless exchange coefficient, and ΔT and Δq are the temperature and specific humidity gradient between the air and surface respectively. In the model, C_E is used as a tuning parameter in both the clean ice SMB model and the debris-covered SMB model (see section 3.1). For simplicity, Q_{LH} over snow and ice surfaces was only calculated when the air temperature had reached ≥ 0°C, at which a saturated surface was assumed (RH_s of 100%), similar to e.g. Bravo et al. (2021). In all other cases, the latent heat flux is set to 0. For debris-covered surfaces, we assume a saturated surface during rainfall, while else Q_{LH} was calculated using the “well mixed boundary layer approach” of Collier et al. (2014).

C) Heat flux by rain

The heat flux provided by rain at the surface is calculated similarly to Sakai et al. (2004):

$$Q_R = \rho_w c_w P \Delta T \tag{8}$$

with ρ_w and c_w the density and specific heat capacity of water, ΔT the temperature difference between the rain and the surface, and P the precipitation rate. For simplicity, the rain temperature T_r is assumed to be equal to the air temperature T_a (Reid and Brock, 2010).

D) Conductive heat flux

The conductive heat flux through the debris layer is derived from the heat conduction equation:

$$Q_c = k_d \frac{\partial T_d}{\partial z} \tag{9}$$

where T_d is the internal debris temperature and k_d the "effective" thermal conductivity:

$$k_d(z) = k_r\big(1 - \phi_d(z)\big) + k_a \phi_d(z) \tag{10}$$

where the "whole rock" thermal conductivity k_r and the surface debris porosity ϕ_d are known from Bozhinskiy et al. (1986). A linear porosity gradient γ_{ϕ_d} hereby accounts for a decrease of the porosity with depth z. For snow and ice surfaces, the conductive heat flux Q_c is put to 0.

E) Surface temperature

The iterative numerical Newton-Raphson method is used to calculate surface temperatures from Eq. (1), similar to Reid and Brock (2010) and Rounce et al. (2018). In the case of a snow or clean ice surface, a maximum threshold of 0°C for T_s is furthermore assigned.

F) Internal debris temperature

The internal debris temperatures are calculated using the thermodynamic heat equation:

$$\rho_d c_d \frac{\partial T_d}{\partial t} = \underbrace{\frac{\partial}{\partial z}\left(k_d \frac{\partial T_d}{\partial z}\right)}_{cconduction} + \underbrace{\rho_w c_w P \left(\frac{\partial T_d}{\partial z}\right)}_{advection} \tag{11}$$

Here, ρ is the density (kg m^{-3}), c the heat capacity (J kg^{-1} K^{-1}), k the thermal conductivity (W m^{-1} K^{-1}), T the temperature and P the precipitation rate (m s^{-1}). The subscripts d and w refer to "effective debris" and "water" properties respectively. We assume that conduction and the heat added or removed by percolating rain are the only processes contributing to changes of the internal debris temperatures, whereas other nonconductive processes, such as phase changes, are assumed to be negligible. The heat equation (Eq. 11) is solved using the numerical Crank-Nicholson scheme (Reid and Brock, 2010; Rounce et al., 2018) and is supplemented by a second order upwind advection scheme for the heat added or removed by rain. The numerical instability of the latter scheme was checked with a Courant–Friedrichs–Lewy (CFL) condition (Smith, 1985).

2.5.2.2 Energy balance at the ice-debris interface

At the vertical ice-debris interface, the energy balance is thus governed by two processes:

$$Q_M^{\downarrow} = Q_C^{\downarrow} + Q_R^{\downarrow} \tag{12}$$

where $Q_C^{\downarrow}$ is the conductive heat flux and $Q_R^{\downarrow}$ is the heat advected by percolating rain water.

A) Conductive heat flux

The conductive heat flux at the ice-debris interface $Q_C^{\downarrow}$ is derived in a similar matter as for the debris surface layer (section 2.5.2.1). However, in this case the internal temperature and thermal conductivity at the base of the debris layer are used in combination with a fixed ice temperature T_i of 0°C at the debris-ice interface.

B) Heat flux by percolating rain

Heat within the debris pack can also be transferred by percolating water ($Q_R^{\downarrow}$). The assumption is made that all rainwater percolates (except the amount that is evaporated at the surface), and that the water temperature of the percolating water equilibrates with that of the debris.

2.5.3 Calculation of melt and runoff

The eventual melt M of snow (M_s), clean ice (M_i) and debris-covered ice (M_d) is calculated by:

$$M = \begin{cases} M_s & if\ h_s > 0 \\ M_i\left(\frac{A_d - A}{A}\right) + M_d\left(\frac{A_d}{A}\right) & if\ h_s = 0 \end{cases} \tag{13}$$

where M_s, M_i and M_d are calculated similarly using the energy available for melt (| meaning ‘or’):

$$\begin{cases} M_s |\ M_i = max\left(0, \frac{Q_M \Delta t}{\rho_w L_m}\right) \\ M_d = max\left(0, \frac{Q_M^{\downarrow} \Delta t}{\rho_w L_m}\right) \end{cases} \tag{14}$$

with L_m the latent heat of fusion, Δt the time step, A_d the debris-covered area, and A the clean ice area (section 2.5.4). On snow and clean ice surfaces, the energy flux available for melting Q_M is calculated from Eq. 1, but in the case of a debris cover, the conductive flux at the base of the debris and the heat added or removed by percolating rainwater provides the energy available for melting $Q_M^{\downarrow}$ (Eq. 12). The corresponding runoff (RO) is as:

$$RO = \begin{cases} W_s & if\ h_s > 0 \\ M_i\ |\ M_d & if\ h_s = 0 \end{cases} \tag{15}$$

Hence, in the case of snow on the surface, runoff is calculated as the meltwater outflow from a saturated snowpack W_s, following the principles of Schaefli and Huss (2011). For snow-free conditions, runoff RO is considered equal to the ice melt by Eqs. 13 to 15.

2.5.4 Fractional debris-covered area

Thin debris rarely forms a continuous cover on the glacier surface, mainly due to redistribution processes (e.g. by meltwater) and a strong variation in the size of the individual debris particles (Fyffe et al., 2020). To account for this phenomenon, a pixel-by-pixel fractional debris-covered area map is derived by performing a maximum likelihood classification on a 3-band Worldview-2 acquisition of the glacier on 31 August 2010, that has a spatial resolution of 0.5 m. The classified grid was resampled to the resolution of the debris thickness map (25 x 25 m), with the mean of all 0.5 x 0.5 m subpixels within a 25 x 25 m pixel as the aggregation method. The best empirical fit for the change of A_d/A with h_d on the glacier exhibited an inverse exponential-type function:

$$\frac{A_d}{A} = 1 - \frac{1}{(5.901 * \ exp(0.0607 * h_d) \ - 5.576} + 0.000286 \qquad (16)$$

where h_d is expressed in cm. Using Eq. 16, A_d/A of a pixel approaches 1 from h_d of ca. 40 cm.

2.6 Model calibration

For model calibration, we minimize the root mean squared error (RMSE) between modelled and observed local surface mass balances. Here, two distinct calibration procedures were carried out: one for clean ice model and one for debris-covered ice model. For the calibration procedure itself, two tuning factors for each distinct model were selected. The results are discussed in section 3.1.

3 Results and discussion

3.1 Model calibration

For the clean ice SMB model, we use observed local surface mass balances in the debris-free areas to tune the model. We select the precipitation gradient γ_P and the turbulent exchange coefficient C_E as tuning parameters, as they are typically hard to directly quantify. Reported values for C_E in the literature for a glacier surface are within the range of 0.001 and 0.004 (e.g. Miles et al., 2017). For the Djankuat Glacier, a minimized RMSE of 0.784 m yr^{-1} w.e. (R^2 = 0.57) was achieved for γ_P= 0.002 m yr^{-1} w.e. m^{-1} and C_E = 0.002 (Fig. 2a, Table 2).

For the debris-covered ice SMB model, C_E was reselected for tuning, which is justified due to the observed significant difference of wind speeds between AWS1 and AWS2 (Fig. 3). Values for C_E over debris are generally within the range of 0.004 to 0.007 in the literature (e.g. Miles et al., 2017). As the thermal and geometrical properties of the debris on the Djankuat Glacier are already known from Bozhinskiy et al. (1986), the second calibration factor is the vertical debris porosity gradient. We assume the porosity to have a value of 0.43 at the debris surface as found by Bozhinskiy et al. (1986), but ϕ_d is reduced with depth by a linear porosity gradient γ_{ϕ_d}. A minimized RMSE of 0.959 m yr^{-1} w.e. (R^2 = 0.31) was achieved for C_E = 0.004 and γ_{ϕ_d} = -0.33 h_d^{-1} (Fig. 2a). The obtained value for the porosity gradient γ_{ϕ_d} corresponds to a porosity at the bottom debris layer of 10%, which is a typical value for unsorted glacial till (e.g. Misra, 2014).

3.2 Model validation

The model performance was checked by comparing the modelled local surface mass balance to local elevation changes as measured by a sonic ranger sensor fixed to the ice. These data show a total lowering of the surface of 3.13 m i.e. (-2.75 m w.e.) between 14 July and 30 September 2009 for AWS1 and 0.55 m i.e. (-0.48 m w.e.) between 9 August 2009 and 25 September 2009 for AWS2. Consequently, the modelled SMB values for AWS1 (-2.91 m w.e.) and for AWS2 (-0.44 m w.e.) agree adequately to the measured ones over the same period (Fig. 2c).

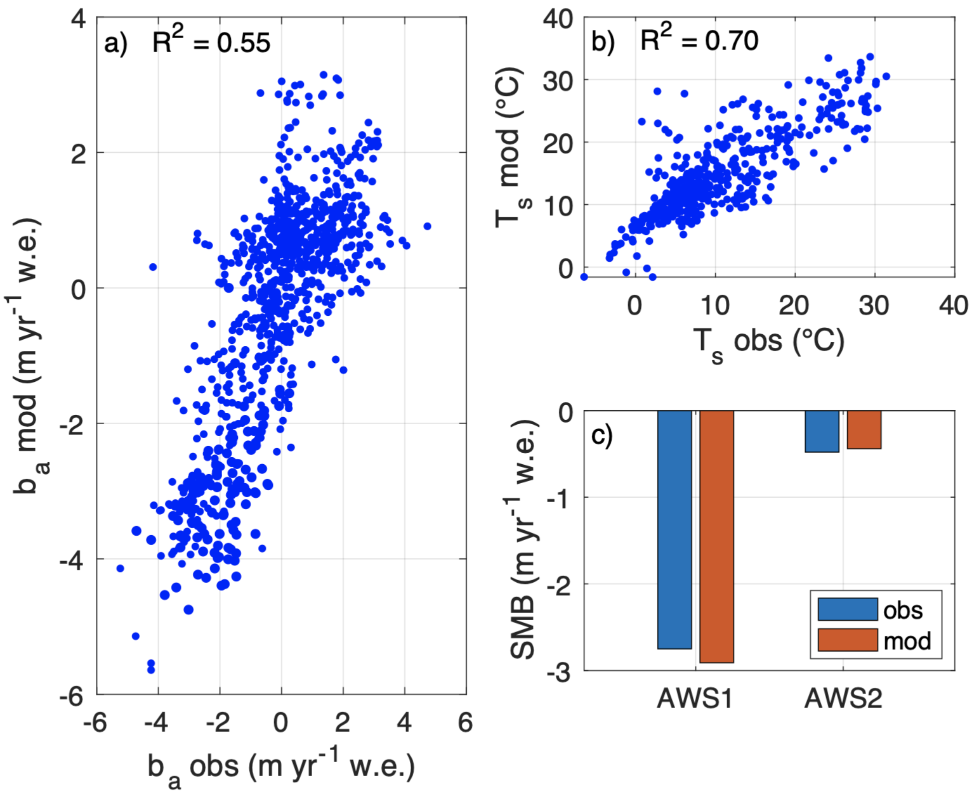

Figure 2. A comparison between the (a) observed vs. best-fit modelled surface mass balances after model calibration, (b) modelled and observed surface temperatures at the AWS2 location, and (c) modelled and observed surface mass balance at the AWS1 and AWS2 locations.

The disappearance of the snow cover for both AWSs was validated by the measured outgoing shortwave radiation (through the surface albedo), as well as by visual inspection of personal pictures and Landsat-5 satellite imagery. For AWS1, $S_{\uparrow}$ was reduced significantly after 14 July 2009, implying that bare ice appeared. At the AWS2 location, however, insufficient data were available to determine the exact date of complete snow disappearance. A Landsat 5 TM image of 11 July 2009, however, shows patches of clean ice and debris around the AWS1 and AWS2 locations, indicating that the snow cover was close to disappearing. The modelled date of bare ice/debris appearance is therefore found to occur in mid-July for both AWSs, which fits to a satisfactory degree with the measured AWS data, the Landsat 5 imagery and pictures by V.V. Popovnin of the glacier taken on 18 July 2009.

The modelled equilibrium line (calculated as the average surface elevation along the 0 m yr^{-1} w.e. contour line of the modelled SMB field) at the end of the ablation season was also checked by comparing it to its observed value. The corresponding value is found to be (3189.96 ± 38.23 m), which is in good agreement with the observed ELA of ca. 3175 m. A final check with respect to the model validation was performed by comparing the modelled and observed outgoing longwave radiation/surface temperatures at the AWS2 location (Fig. 2b), which likewise showed an adequate correlation (R^2 = 0.70). Hence, despite the lack of additional and more extensive validation data, the findings above indicate that the model performs satisfactory well.

Table 2. Parameters, variables, and physical constants used in the model.

Supraglacial debris-related properties and model variables					
Variable	**Symbol**	**Unit + value**	**Variable**	**Symbol**	**Unit + value**
Debris thickness	h_d	m	Debris emissivity	ε_d	0.90
Ddebris sublayer thickness	h	m	Debris albedo	α_d	0.10
Number of calculated debris layers	N	h_d/h	Debris turbulent exchange coefficient	C_E	0.004
Rock thermal conductivity	k_r	2.8 W m^{-1} K^{-1}	Characteristic snow depth for debris	h_d^s	0.03 m
Rock density	ρ_r	2600 kg m^{-3}	Effective debris thickness	h_d^e	0.03 m
Debris (surface) porosity	ϕ_d	0.43	Critical debris thickness	h_d^c	0.09 m
Debris porosity gradient	γ_{ϕ_d}	-0.33 h_d^{-1}	Characteristic debris thickness	h_d^*	0.44 m
Rock specific heat capacity	c_r	1260 J K^{-1} kg^{-1}	Debris-covered area	A_d	m^2
Rock volumetric heat capacity	$\rho_r c_r$	3 276 000 J m^{-3} K^{-1}	Fractional debris-covered area	A_d/A	m^2 m^{-2}
Other constants used in the model					
Constant	**Symbol**	**Unit + value**	**Constant**	**Symbol**	**Unit + value**
Gravitational acceleration	g	9.81	Ice density	ρ_i	880 kg m^{-3}
Stefan-Boltzmann constant	σ	5.67*10^{-8} W m^{-2} K^{-4}	Surface emissivity of snow and ice	ε_s	0.97
Latent heat of vaporization of water	L_v	2.20*10^6 J kg^{-1}	Albedo ice	α_i	0.21
Latent heat of fusion water	L_m	3.34*10^5 J kg^{-1}	Albedo snow	α_s	0.77
Density air	ρ_a	1.29 kg m^{-3}	Threshold rain/snow distinction	T_{thr}	2 °C
Density water	ρ_w	1000 kg m^{-3}	Vertical precipitation gradient	γ_P	0.002 m yr^{-1} m^{-1}
Specific heat capacity air	c_a	1010 J K^{-1} kg^{-1}	Ice/snow turbulent exchange coefficient	C_E	0.002
Specific heat capacity water	c_w	4184 J K^{-1} kg^{-1}	Characteristic snow depth ice surface	d_i^*	0.011 m
Model time step	Δt	10800 s	Model spatial resolution	Δx	25 m
Air thermal conductivity	k_a	0.024 W m^{-1} K^{-1}	Water thermal conductivity	k_w	0.57 W m^{-1} K^{-1}

3.3 Comparison of surface conditions over clean ice and debris-covered ice

3.3.1 Meteorological variables

Surface temperatures T_s are not directly measured by the AWSs but can be derived from $L_\uparrow$. T_s is fixed at 0°C for melting conditions at the AWS1 location (-0.5°C on average during the summer season), whereas the average T_s at the AWS2 is calculated to be 9.2°C during the same period (Table 3, Fig. 3a and c). The surface humidity also differs significantly: over clean ice, the surface is saturated during the summer when T_a > 0°C (RH_s= 100%), whereas RH_s drops to nearly 35% on average at noon over the debris at the AWS2 location (Fig. 3b and d). On average, RH_s was notably lower at the AWS2 location during the summer period (AWS1: 98.6% and AWS2: 64.9%).

A noticeable dissimilarity can be noted with respect to the wind regime. In fact, the wind speed u recorded by AWS2 is, on average, reduced by ca. 50% (Δu = 1.9 m s^{-1}, R2 = 0.33) when compared to AWS1 over the same period (Table 3, Fig. 3b and d). Such a reduction of u over debris-covered terrain has been noted on other glaciers, and is therefore consistent with other studies (e.g. Yang et al., 2017; Nicholson and Stiperski, 2020). Valid explanations for this phenomenon include an increased surface roughness (e.g. Miles et al., 2017) and/or the modification of katabatic glacier winds over the debris, with interference of anabatic or convection patterns (e.g. Shaw et al., 2016; Yang et al., 2017). Also the placement of the AWS2, which is closer to the valley slopes and to the Mount Uya-tau peak, may (partly) explain the decrease of u due to shielding effects. Wind data from AWSs showed the dominance of a katabatic wind regime for both AWS locations, which implies that the katabatic flow penetrates over the debris-covered part of the Djankuat Glacier. This indicates that the resistance from anabatic/convective wind regimes is not sufficient to break down the katabatic wind. This observation is remarkable, as katabatic wind regimes are thought to rapidly break down after penetrating debris-covered terrain (e.g. Potter et al., 2020). Possible explanations for this phenomenon may be the relatively large and steep bare ice area up-glacier of the AWS2 location, providing the katabatic flow with a high along-slope momentum, and/or the fact that AWS2 was situated relatively close to the horizontal ice-debris margin (Fig. 1). Unfortunately, more data to further investigate this pattern were lacking.

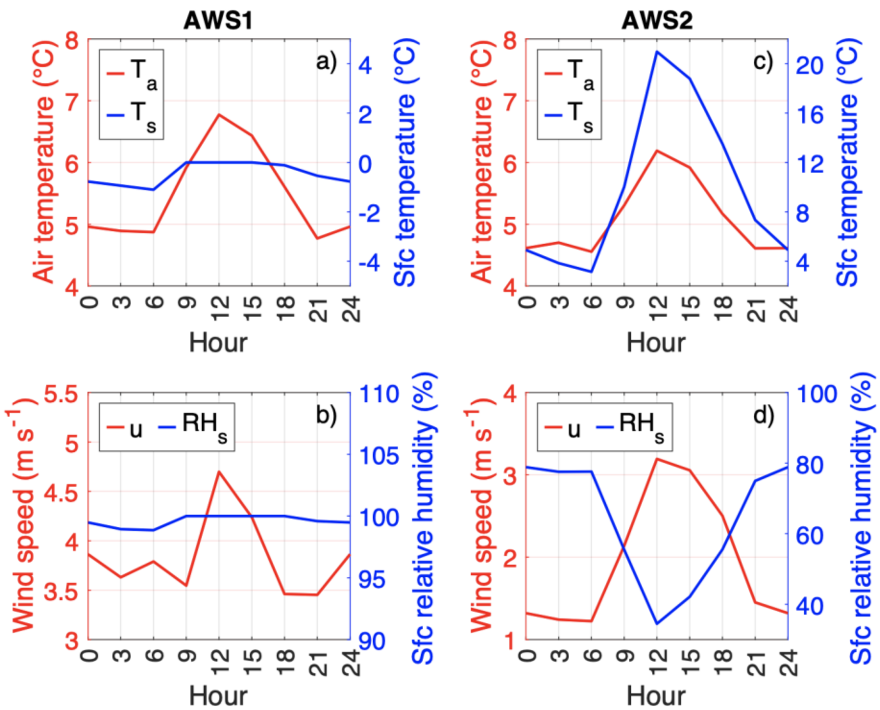

Figure 3. A comparison of average meteorological variables during the summer season (June-September) at the (a) and (c) the AWS1 (clean ice), and (b) and (d) the AWS2 (debris-covered ice) location.

3.3.2 Energy and mass balance components

The calibrated energy and mass fluxes on a sub-daily and (sub-)annual basis for the AWS1 (h_d = 0 cm, A_d/A = 0) and AWS2 (h_d = 43 cm, A_d/A = 1) locations are shown in Figs. 4 to 6. The spatially distributed energy (for June to September, JJAS) and mass (for the entire 2008/09 measurement year) fluxes are shown in Fig. 7.

The net shortwave radiation Q_S exhibits a clear intra-daily and intra-yearly oscillation. During the summer, the average Q_S is somewhat higher over the debris-covered terrain then over the clean ice surface, which is mostly related to a lower surface albedo (Table 2). Net longwave fluxes Q_L are generally negative and act as an energy sink over both surface types. However, $L_\uparrow$ reaches a fixed maximum value of ca. 316 W m^{-2} during snow/ice melt, whereas Q_L becomes increasingly negative over a debris-covered ice surface (on average -73.8 W m^{-2} for AWS2 compared to -40.7 W m^{-2} for AWS1). The turbulent fluxes are clearly positive during the ablation season for the AWS1 location, as air temperature generally exceeds the fixed surface temperature of a saturated, melting surface. However, for an exposed debris-covered surface, the turbulent heat fluxes become increasingly negative due to relatively warmer and drier surfaces (Figs. 4 and 5, Table 3). Overall, the turbulent fluxes therefore generally act as energy sources over snow/ice and as energy sinks over debris-covered terrain. The conductive heat flux is non-existent for snow/ice surfaces in the model and are clearly negative for debris surfaces during the ablation season (on average -37.9 W m^{-2} for AWS2). At last, the heat flux added by rain Q_R is less important, but generally acts as a small energy source over snow/ice (on average 1.3 W m^{-2}) and as an energy sink over debris (on average -1.2 W m^{-2}) (Table 3). As such, for both AWS locations, the incoming solar and longwave radiation ($S_{\downarrow}$+ $L_{\downarrow}$) are incoming energy sources. For a snow/ice surface, $S_{\downarrow}$ and $L_{\downarrow}$ are mainly used, together with Q_{SH} and Q_{LH}, for the melting of snow and ice. Over debris-covered terrain, $S_{\downarrow}$ and $L_{\downarrow}$ heat the debris-covered surface, whereas $S_{\uparrow}$, $L_{\uparrow}$, Q_{SH}, Q_{LH} and Q_C generally provide the energy output. The corresponding daily cycle of the mass fluxes over debris-covered ice is furthermore highly attenuated with depth and retarded with respect to the timing of the maximum of the surface energy balance (Fig. 4d).

When comparing the evolution of the corresponding mass balance components throughout the measurement year, both AWS locations are found to produce similar runoff values during the largest part of the measurement year. In this case, practically all runoff is accounted for by the outflow of the retained meltwater from the snowpack ($RO \approx W_s$). Once snow has melted, the supraglacial debris cover significantly alters the melting of the underlying ice and modifies the total runoff and the eventual mass balance ($RO \approx M$, Fig. 6). Consequently, total runoff is significantly reduced at the AWS2 site (3.0 m w.e. yr^{-1}, from which 23% ice melt) when compared to the AWS1 (5.1 m w.e. yr^{-1}, from which 57% ice melt).

Table 3. Average meteorological variables, average energy fluxes and year-round mass fluxes at the AWS1 and AWS2 locations during the 2008/09 measurement year at the Djankuat Glacier. Here, JJAS depicts the period from June to September.

	AWS1	AWS2
Meteorological variables (JJAS)		
T_a	5.5°C	5.1°C
T_s	-0.5°C	9.2°C
u	3.8 m s^{-1}	1.9 m s^{-1}
RH_a	73.1%	72.5%
RH_s	98.6%	64.9%
Energy balance components (JJAS)		
Q_S	163.8 W m^{-2}	212.3 W m^{-2}
Q_L	-40.7 W m^{-2}	-73.8 W m^{-2}
Q_{SH}	67.7 W m^{-2}	-94.8 W m^{-2}
Q_{LH}	2.2 W m^{-2}	-4.5 W m^{-2}
Q_C	0.0 W m^{-2}	-37.9 W m^{-2}
Q_R	1.3 W m^{-2}	-1.2 W m^{-2}
Q_M	-194.2 W m^{-2}	-66.9 W m^{-2}
Mass balance components (measurement year)		
RO	5.1 m yr^{-1} w.e.	3.0 m yr^{-1} w.e.
ACC	2.2 m yr^{-1} w.e.	2.3 m yr^{-1} w.e.
b_a	-2.9 m yr^{-1} w.e.	-0.7 m yr^{-1} w.e.

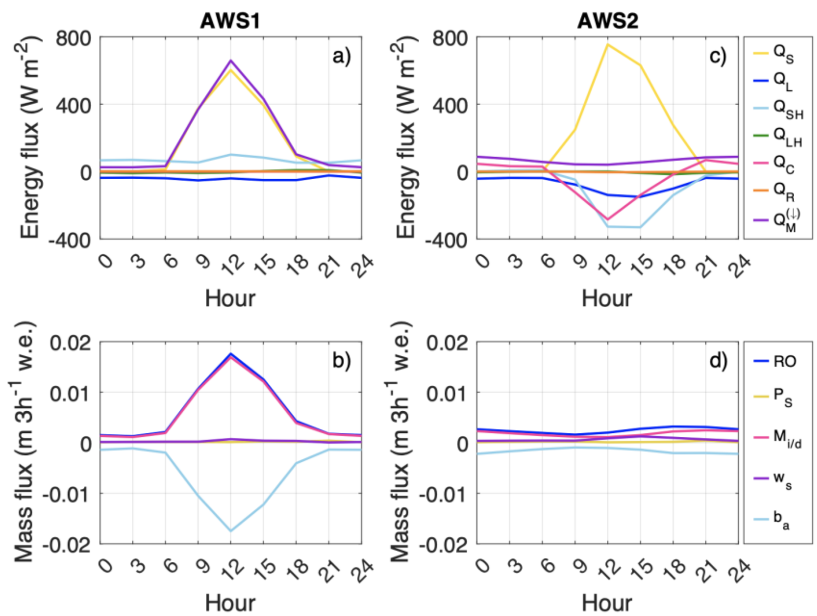

Figure 4. Average diurnal cycle of surface energy and mass balance components at the (a) and (b) AWS1 (clean ice), and (c) and (d) AWS2 (debris-covered ice) locations during the summer (JJAS) of the 2008/09 measurement year on the Djankuat Glacier. Energy for melting in (c) and ice melt/runoff in (d) show the fluxes at the debris-ice interface.

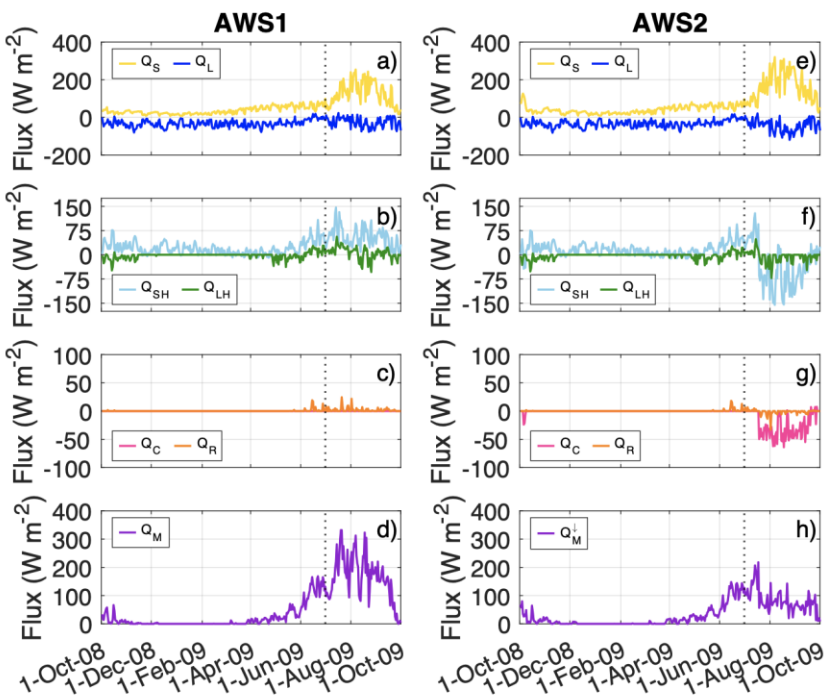

Figure 5. Comparison of the temporal evolution of the daily averaged surface energy fluxes during the 2008/09 measurement year on the Djankuat Glacier at the (left) AWS1 (clean ice), and (right) AWS2 (debris-covered ice) locations. The dashed vertical line shows the onset of the AWS operational period. Energy for melting in (h) shows the flux at the debris-ice interface.

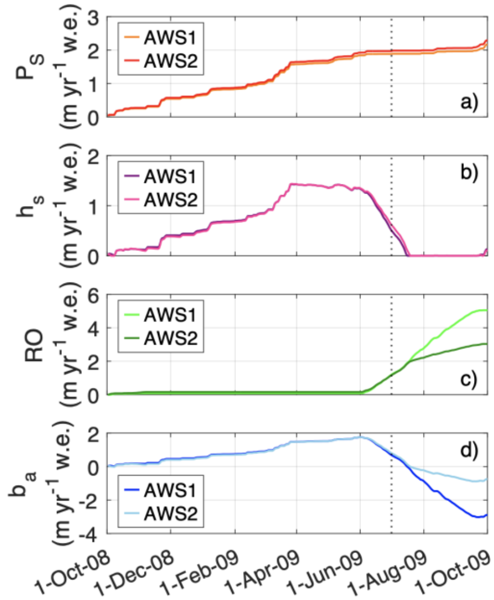

Figure 6. The modelled temporal evolution of the mass balance components of the Djankuat Glacier at the AWS1 and AWS2 location throughout the 2008/09 balance year.

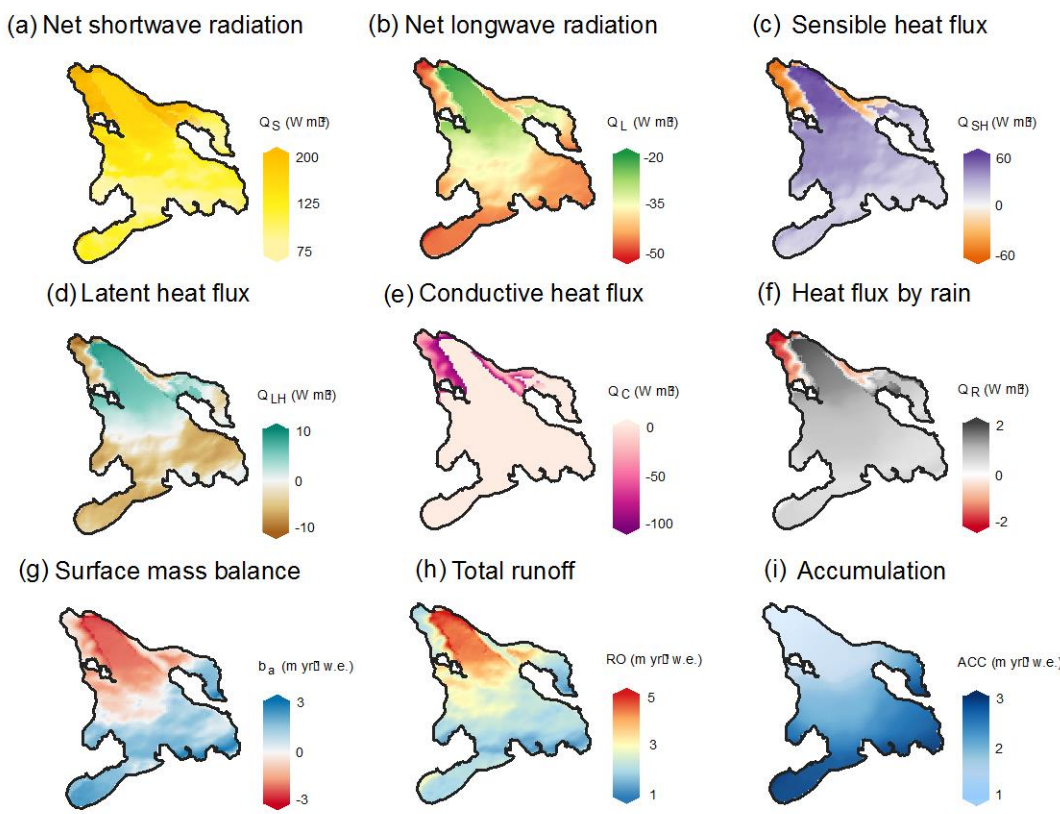

Figure 7. Spatial distribution of (upper and middle row) average JJAS surface energy fluxes, and (lower row) surface mass balance components during the entire 2008/09 measurement year at the Djankuat Glacier.

3.3.3 Effect of debris thickness and fractional debris-covered area

In Fig. 8a, the energy fluxes during the summer period (JJAS) at the AWS2 pixel are plotted against different “hypothetical” values for the debris thickness h_d, with the assumption of a consistent full debris cover (A_d/A = 1). Especially the conductive heat flux is modelled to increase drastically for a higher h_d (-193.7 W m^{-2} for h_d = 1 cm to -13.4 W m^{-2} for h_d = 200 cm), which is a consequence of increasing surface temperatures. Q_L is consistently negative but its value decreases slightly with an increasing h_d due to a higher $L_{\uparrow}$, which is as well related to a higher T_s. For thin debris, Q_{SH} and Q_{LH} are slightly positive on average, but these fluxes quickly switch sign to act as an energy sink rather than an energy source. The pattern of change of the energy for melt indicates that higher net radiation and turbulent heat fluxes (Q_L+Q_{SH}+Q_{LH}), but especially the higher temperature gradient over vertical distance (i.e. less heat storage potential and lower insulating effects as captured by the highly negative conductive heat flux Q_C), are the main drivers of high sub-debris melt rates if debris is thin. Consequently, melt enhancement occurs for thin debris, as ice melt rates are modelled to increase indefinitely for a decreasing debris thickness (Fig. 8b). For thicker debris, melt suppression becomes increasingly notable, as the net radiation and turbulent heat fluxes (Q_L+Q_{SH}+Q_{LH}) decrease, and Q_C flattens off towards 0.

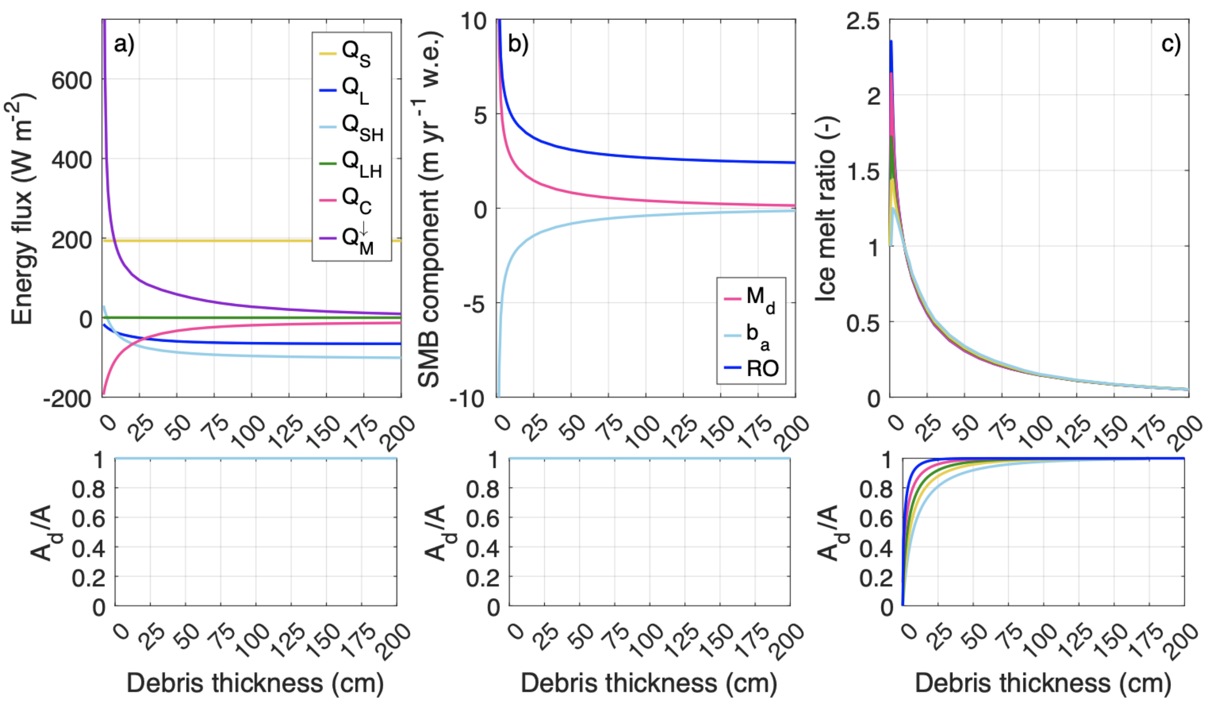

Figure 8. The modelled effect of a varying “hypothetical” debris thickness and fractional debris-covered area on the mass and energy balance components of the Djankuat Glacier at the AWS2 pixel. Subplots show (a) the average JJAS surface energy fluxes, (b) the whole-year mass fluxes as a function of debris thickness and (c) the effect of an arbitrarily varying rate of the increase of the fractional debris-covered area with debris thickness on the ice melt ratio (M_d/M_i).

The effect of the debris-covered area on the local surface mass balance at the AWS2 location is, at last, shown in Fig. 8c. Here, the “hypothetical” fractional debris-covered area is modelled to increase with h_d at arbitrarily varying rates, starting from A_d/A = 0 for bare ice surfaces. The inclusion of this process allows the melt-debris thickness relationship to exhibit a clear maximum, from which the magnitude depends on the rate of increase of the debris-covered area with h_d. If the debris-covered area increases rapidly with debris thickness ($\partial(A_d/A)/\partial h_d$ is high), the melt enhancement effect is most pronounced. This finding is related to Eq. 13 as in that case, a larger weight is given to the debris-covered melt when compared to the bare ice melt (which is relatively lower for thin debris). For lower rates of $\partial(A_d/A)/\partial\, h_d$, the melt enhancement is less notable since larger weights are given to the relatively lower clean-ice melt for thin debris (Fig. 8c). Interestingly, considering the patchiness of the debris cover through Eq. 13 thus allows the model to simulate a distinct maximum melt enhancement for thin debris, after which a gradual melt suppression occurs when h_d further increases. As noted by Reid and Brock (2010), the inclusion of the patchiness of the debris may (whether or not partly) explain the occurrence of a maximum melt enhancement for thin debris in the Østrem curve. This will also be further explored in the accompanying paper Verhaegen et al. (subm.).

4 Model limitations, uncertainties and recommandations

4.1 Spatialization methods

With respect to the wind spatialization method, we note that the distinction between synoptic-scale winds and the thermally-driven local glacier winds is not made when supplementing the AWS time series with ERA5-Land data. Rather, wind data from the overlapping part of the AWS and ERA5-Land data are used to create a continuous time series, regardless of the wind regime. The onset and prevalence of these thermally-driven winds is deemed complex and hard to implement into the model. Wind conditions on the glacier may be further complicated by interference of warm up-valley winds, convective processes over debris, and topographic features (e.g. Van den Broeke, 1997; Oerlemans and Grisogono, 2002; Potter et al., 2020; Shaw et al., 2021). However, thermal wind regimes have been shown to significantly influence the momentum, heat and moisture budgets of a glacier's near-surface boundary layer, which justifies the need to include thermally-driven wind regimes into spatially distributed glacier models.

Steiner and Pellicciotti (2016), at last, found that the air temperature over debris-covered terrain was notably higher (even up to 2°C in extreme cases) than those predicted by a temperature lapse rate over clean ice. In our model, this process is neglected as we have no further information as to which proportion of the temperature difference between both AWSs is caused by the presence of debris.

4.2 Distributed energy and mass balance modelling

The calculation of the incoming shortwave and longwave radiation could be further supplemented with additional processes, which have been neglected in our study for simplicity. For example, shortwave radiation can additionally be affected by multiple reflection between the atmosphere and the surface (e.g. Rybak et al., 2021), and also the incoming longwave radiation at the glacial surface can be affected by reflections from the surrounding terrain. The sky transmissivity is kept constant in space for each time step, whereas earlier studies have noted that the transmissivity can exhibit a dependence on the elevation (e.g. Oerlemans, 2001), as well as for e.g. spatial variations of cloud cover (e.g. Iqbal, 1983).

With respect to the latent heat flux parameterization, several strategies have been implemented in the literature to deal with the often-immeasurable surface humidity of a debris-covered surface (e.g. Nakawo and Young, 1982; Fujita and Sakai, 2014; Rounce and McKinney, 2014; Rounce et al., 2015; Rounce et al., 2018). Collier et al. (2014) calculated Q_{LH} based upon a well-mixed boundary layer assumption between the debris and the AWS, which is the method of choice in our study. The selected latent heat flux parameterization is modelled to not have a significant influence on the eventual results in our study. The only significant modification is achieved when assuming an unrealistic constantly saturated debris surface, where RH_s = 100% throughout the whole ablation season. In that case, significantly less melt occurs because more energy is used for evaporation rather than for surface warming. This phenomenon will be further investigated in the accompanying paper Verhaegen et al. (subm.) for the Djankuat glacier.

We acknowledge that a more extensive validation dataset would benefit the credibility of our model. An additional AWS may have increased the quality of our model, especially over complex areas such as the horizontal ice-debris margin. Surface temperatures can be utilized for model validation as well, but the available Landsat 5 satellite acquisitions during the summer of 2009 exhibit too low quality to be used in a validation procedure.

5 Conclusions

In this study, a spatially distributed and physically based 2D surface energy and mass balance model at high spatial (25 m) and temporal (3-hourly) resolution was used to simulate the spatio-temporal distribution of meteorological variables, energy fluxes and mass balance components over both the clean ice and debris-covered ice surfaces of the Djankuat Glacier, a WGMS reference glacier situated in the Caucasus (Russian Federation). The main results show that:

- The driving factors determining the spatial variability of meteorological variables and surface energy/mass fluxes over the glacier surface are a combination of the topography (elevation, slope and aspect) and the surface characteristics (albedo, emissivity and roughness).

- The changing near-surface wind and surface temperature/moisture regimes over debris-covered ice are found to significantly alter the surface energy balance and the extent of momentum, heat, and moisture exchanges between the atmosphere and the glacier surface.

- The eventual effect of supraglacial debris on the energy/mass fluxes and sub-debris ice melt depends on the debris thickness and the debris-covered area. For thin/patchy debris, melt is enhanced when compared to clean ice areas due to a decreased surface albedo, a fast conduction of heat to the ice surface, and additional energy input from the turbulent heat fluxes. For thick/continuous debris, melt is significantly suppressed because the diurnal cycle of the net energy flux becomes increasingly attenuated with depth.

In conclusion, this work presents an approach for the spatio-temporalization of meteorological data and the comparison of the meteorology and the surface energy and mass fluxes of clean ice and debris-covered terrain, which is crucial in determining the effect of supraglacial debris on glacier melt patterns and its climate change response. Because a 2D glacier-wide direct comparison between clean ice and debris-covered terrain is not straightforward, its application is still absent in the literature. However, the long monitoring program and abundant data availability for the Djankuat Glacier forwarded this specific glacier as an ideal candidate for the study. Although improvements can certainly be made (e.g. the separation of thermally-driven and synoptic-scale wind regimes and the need for more extensive validation data), our model produces a good agreement between simulated and observed melt rates. The results of this study contribute to the knowledge of how debris-related modified melt and runoff might affect the future supply of water for drinking, irrigation and/or hydroelectric energy generation, as well as the threat of flooding events, glacial debris flows, and glacial lake outbursts of (partly) debris-covered glaciers.

Figure captions

Figure 1. Sketch of the Djankuat Glacier for 2010 conditions with debris thickness map (Popovnin et al., 2015) and AWS locations (Rets et al., 2019).

Figure 2. A comparison between the (a) observed vs. best-fit modelled surface mass balances after model calibration, (b) modelled and observed surface temperatures at the AWS2 location, and (c) modelled and observed surface mass balance at the AWS1 and AWS2 locations.

Figure 3. A comparison of average meteorological variables during the summer season (JJAS) at the (a) and (c) the AWS1 (clean ice), and (b) and (d) the AWS2 (debris-covered ice) location.

Figure 4. Average diurnal cycle of surface energy and mass balance components at the (a) and (b) AWS1 (clean ice), and (c) and (d) AWS2 (debris-covered ice) locations during the summer (JJAS) of the 2008/09 measurement year on the Djankuat Glacier. Energy for melting in (c) and ice melt/runoff in (d) show the fluxes at the debris-ice interface.

Figure 5. Comparison of the temporal evolution of the daily averaged surface energy fluxes during the 2008/09 measurement year on the Djankuat Glacier at the (left) AWS1 (clean ice), and (right) AWS2 (debris-covered ice) locations. The dashed vertical line shows the onset of the AWS operational period. Energy for melting in (h) shows the flux at the debris-ice interface.

Figure 6. The modelled temporal evolution of the mass balance components of the Djankuat Glacier at the AWS1 and AWS2 location throughout the 2008/09 balance year.

Figure 7. Spatial distribution of (upper and middle row) average JJAS surface energy fluxes, and (lower row) surface mass balance components during the entire 2008/09 measurement year at the Djankuat Glacier.

Figure 8. The modelled effect of a varying "hypothetical" debris thickness and fractional debris-covered area on the mass and energy balance components of the Djankuat Glacier at the AWS2 pixel. Subplots show (a) the average JJAS surface energy fluxes, (b) the whole-year mass fluxes as a function of debris thickness and (c) the effect of an arbitrarily varying rate of the increase of the fractional debris-covered area with debris thickness on the ice melt ratio (M_d/M_i).

Acknowledgments

O. Rybak and V. Popovnin were supported by the Russian Science Foundation grant No. 22-17-00133. Y. Verhaegen was supported by the Copernicus Climate Change Service (C3S), which is implemented by the European Centre for Medium-Range Weather Forecasts (ECMWF) on behalf of the European Commission. The authors declare that they have no conflict of interest.

Data availability statement

The AWS data used for this study are available as open access products via the PANGAEA repository of Rets et al. (2019) (https://doi.org/10.1594/PANGAEA.894807). The model code was written in MATLAB_R2022a. It can be found and downloaded from https://github.com/yoniv1/Djankuat_Ostrem_curve (last access: 27 February 2023). (https://doi.org/10.5281/zenodo.7451031, Verhaegen and Huybrechts, subm.).

References

Allen, R. G., Trezza, R., and Tasumi, M. (2006). Analytical integrated functions for daily solar radiation on slopes, Agr. Forest Meteorol., 139, 55–73, https://doi.org/10.1016/j.agrformet.2006.05.012.

Ayala, A., Pellicciotti, F., Peleg, N., and Burlando, P. (2017). Melt and surface sublimation across a glacier in a dry environment: distributed energy-balance modelling of Juncal Norte Glacier, Chile, J. Glaciol., 63, 803–822, https://doi.org/10.1017/jog.2017.46.

Bozhinskiy, A. N., Krass, M. S., and Popovnin, V. V. (1986). Role of debris cover in the thermal physics of glaciers, J. Glaciol., 32, 255–266, https://doi.org/10.3189/S0022143000015598.

Bravo, C., Ross, A. N., Quincey, D. J., Cisternas, S., and Rivera, A. (2021). Surface ablation and its drivers along a west–east transect of the Southern Patagonia Icefield, J. Glaciol., 1–14, https://doi.org/10.1017/jog.2021.92.

Carenzo, M., Pellicciotti, F., Mabillard, J., Reid, T., and Brock, B. W. (2016). An enhanced temperature index model for debris-covered glaciers accounting for thickness effect, Adv. Water Resour., 94, 457–469, https://doi.org/10.1016/j.advwatres.2016.05.001.

Collier, E., Nicholson, L. I., Brock, B. W., Maussion, F., Essery, R., and Bush, A. B. G. (2014). Representing moisture fluxes and phase changes in glacier debris cover using a reservoir approach, The Cryosphere, 8(4), 1429–1444, https://doi.org/10.5194/tc-8-1429-2014.

Duffie, J. A. and Beckman, W. A. (2006). Solar thermal energy processes, Wiley Interscience, New York, 944 pp..

Fujita, K. and Sakai, A. (2014). Modelling runoff from a Himalayan debris-covered glacier, Hydrol. Earth Syst. Sci., 18, 2679–2694, https://doi.org/10.5194/hess-18-2679-2014.

Gabbi, J., Carenzo, M., Pellicciotti, F., Bauder, A., and Funk, M. (2014). A comparison of empirical and physically based glacier surface melt models for long-term simulations of glacier response, J. Glaciol., 60, 1140–1154, https://doi.org/10.3189/2014JoG14J011.

Gascoin, S., Lhermitte, S., Kinnard, C., Borstel, K., and Liston, G. (2013). Wind effects on snow cover in Pascua-Lama, Dry Andes of Chile. Advances in Water Resources, Elsevier, 55, 25-39, https://doi.org/10.1016/j.advwatres.2012.11.013.

Giese, A., Boone, A., Wagnon, P., and Hawley, R. (2020). Incorporating moisture content in surface energy balance modeling of a debris-covered glacier, The Cryosphere, 14(5), 1555–1577, https://doi.org/10.5194/tc-14-1555-2020.

Hagg, W., Shahgedanova, M., Mayer, C., Lambrecht, A., and Popovnin, V. V. (2010). A sensitivity study for water availability in the Northern Caucasus based on climate projections, Glob. Planet. Change, 73, 161–171, https://doi.org/10.1016/j.gloplacha.2010.05.005.

Harris, A. (2013). Thermal Remote Sensing of Active Volcanoes: A User's Manual, Cambridge University Press, Cambridge, 345 pp.

Huo, D., Chi, Z., and Ma, A. (2021). Modeling Surface Processes on Debris-Covered Glaciers: A Review with Reference to the High Mountain Asia, Water 2021, 13, 101, https://doi.org/10.3390/w13010101.

Huss, M. and Hock, R. (2015). A new model for global glacier change and sea-level rise, Front. Earth Sci., 3, 1–22, https://doi.org/10.3389/feart.2015.00054.

Iqbal, M. (1983). An introduction to solar radiation, Academic Press, Toronto, 390 pp.

Jouvet, G., Huss, M., Funk, M., and Blatter, H. (2011). Modelling the retreat of Grosser Aletschgletscher, Switzerland, in a changing climate, J. Glaciol., 57, 1033–1045, https://doi.org/10.3189/002214311798843359.

Kirkbride, M. P. (2000). Ice-marginal geomorphology and Holocene expansion of debris-covered Tasman Glacier, New Zealand. Debris-Covered Glaciers, Proceedings of a workshop held at Seattle, Washington, USA, September 2000, 264, 211–217, https://doi.org/10.1007/978-90-481-2642-2_622.

Lejeune, Y., Bertrand, J.-M., Wagnon, P., and Morin, S. (2013). A physically based model of the year-round surface energy and mass balance of debris-covered glaciers, J. Glaciol., 59, 327–344, https://doi.org/10.3189/2013JoG12J149.

Liston, G., and Elder., K. (2006). A meteorological distribution system for high-resolution terrestrial modeling (MicroMet). J. Hydrometeorol., 7, 217–234, https://doi.org/10.1175/JHM486.1.

Liston, G., and Sturm, M. (1998). A snow-transport model for complex terrain, J. Glaciol., 44(148), 498–516, https://doi.org/10.3198/1998JoG44-148-498-516.

Liston G.E., Haehnel R.B., Sturm M., Heimstra A., Berezovskaya S., Tabler R.D. (2007). Simulating complex snow distributions in windy environments using SnowTran-3D, Journal of Glaciology, 53(181), 241-256), https://doi.org/10.3189/172756507782202865.

Masson-Delmotte, V., Zhai, P., Pirani, A., Connors, S., Péan, C., Berger, S., Caud, N., Chen, Y., Goldfarb, L., Gomis, M., Huang, M., Leitzell, K., Lonnoy, E., Matthews, J., Maycock, T., Waterfield, T., Yelekçi, O., Yu, R., and Zhou, B. E. (2021). Summary for Policymakers., In: Climate Change 2021: The Physical Science Basis. Contribution of Working Group I to the Sixth Assessment Report of the Intergovernmental Panel on Climate Change., IPCC, Cambridge University Press.

Maussion, F., Scherer, D., Mölg, T., Collier, E., Curio, J., and Finkelnburg, R (2014). Precipitation Seasonality and Variability over the Tibetan Plateau as Resolved by the High Asia Reanalysis, Journal of Climate, 27(5), 1910-1927, https://doi.org/10.1175/JCLI-D-13-00282.1.

Mernild, S. H., Liston, G., Hiemstra, C. A., Malmros, J. K., Yde, J. C., and McPhee, J. (2017). The Andes Cordillera. Part I: snow distribution, properties, and trends (1979–2014), Int. J. of Clim., 37, 1680-1698, https://doi.org/10.1002/JOC.4804.

Miles, E. S., Steiner, J. F., and Brun, F. (2017). Highly variable aerodynamic roughness length (z0) for a hummocky debris-covered glacier, J. Geophys. Res: Atmospheres, 122, 16, 8447-8466, https://doi.org/10.1002/2017JD026510.

Milles, E. S., Steiner J. F., Buri, P., Immerzeel, W. W., and Pelliciotti, F. (2022). Controls on the relative melt rates of debris-covered glacier surfaces, Environ. Res. Lett., 17, 064004, https://doi.org/10.1088/1748-9326/ac6966.

Misra, A. K. (2014). Engineering geology, S. Chand & Company Limited, New Delhi, 248 pp.

Morozova, P. A. and Rybak, O. (2017). Downscaling of the global climate model data for the mass balance calculation of mountain glaciers, Ice and Snow, 57(4), 437–452, https://doi.org/10.15356/2076-6734-2017-4-437-452.

Muñoz-Sabater, J. (2019). ERA5-Land hourly data from 1981 to present, Copernicus Climate Change Service (C3S) Climate Data Store (CDS) [data set], https://doi.org/10.24381/cds.e2161bac.

Nakawo, M., and Young, G. J. (1982). Estimation of glacier ablation under a debris layer from surface temperature and meteorological variables, J. Glaciol., 28 (92), 29–34.

Nemec, J., Huybrechts, P., Rybak, O., and Oerlemans, J. (2009). Reconstruction of the annual balance of Vadret da Morteratsch, Switzerland, since 1865, Ann. Glaciol., 50, 126–134, https://doi.org/10.3189/172756409787769609.

Nicholson, L. and Stiperski, I. (2020). Comparison of turbulent structures and energy fluxes over exposed and debris-covered glacier ice, J. Glaciol., 66(258), 1–13, https://doi.org/10.1017/jog.2020.23.

Oerlemans, J. and Grisogono, B. (2002). Glacier winds and parameterisation of the related surface heat fluxes, Tellus, 54(5), 440-452, https://doi.org/10.3402/tellusa.v54i5.12164.

Oerlemans, J. (2001). Glaciers and climate change, A. A. Balkema Publishers, Lisse, 160 pp.

Oerlemans, J. and Knap, W. H. (1998). A 1-year record of global radiation and albedo in the ablation zone of Marteratschgletscher, Switzerland, J. Glaciol., 44, 231–238, https://doi.org/10.3189/S0022143000002574.

Østrem, G. (1959). Ice melting under a thin layer of moraine, and the existence of ice cores in moraine ridges, Geogr. Ann., 41, 228–230.

Paterson, W. (1994). The physics of glaciers, 3rd Edition, Butterworth Heinemann, Oxford, 481 pp.

Popovnin, V. V. and Naruse, R. (2005). A 34-year long record of mass balance and geometric changes of the Djankuat Glacier, Caucasus, Bull. Glaciol. Res., 22, 121–133.

Popovnin, V. V. and Pylayeva T. V. (2015). Avalanche feeding of Djankuat Glacier, Ice and snow, 55, 21–32, https://doi.org/10.15356/2076-6734-2015-2-21-32 (in Russian).

Popovnin, V. V., Rezepkin, A. A., and Tielidze, L. G. (2015). Superficial moraine expansion on the Djankuat glacier snout over the direct glaciological monitoring period, Earth's Cryosphere, 19, No. 1, 79–87 (in Russian).

Potter, E. R., Orr, A., Willis, I. C., Bannister D., and Wagnon, P. (2020). Meteorological impacts of a novel debris-covered glacier category in a regional climate model across a Himalayan catchment, Atmos Sci Lett., 22(3), https://doi.org/10.1002/asl.1018.

Reid, T. D. and Brock, B. W. (2010). An energy-balance model for debris-covered glaciers including heat conduction through the debris layer, J. Glaciol., 56, 903–916, https://doi.org/10.3189/002214310794457218.

Rets, E. P., Popovnin, V. V., Toropov, P. A., Smirnov, A. M., Tokarev, I. V., Chizhova, J. N., Budantseva, N. A., Vasil'chuk, Y. K., Kireeva, M. B., Ekaykin, A. A., Veres, A. N., Aleynikov, A. A., Frolova, N. L., Tsyplenkov, A. S., Poliukhov, A. A., Chalov, S. R., Aleshina, M. A., and Kornilova, E. D. (2019). Djankuat glacier station in the North Caucasus, Russia: a database of glaciological, hydrological, and meteorological observations and stable isotope sampling results during 2007–2017, Earth Syst. Sci. Data, 11, 1463–1481, https://doi.org/10.5194/essd-11-1463-2019.

Rounce, D. R., and McKinney, D. C. (2014). Debris thickness of glaciers in the Everest area (Nepal Himalaya) derived from satellite imagery using a nonlinear energy balance model, The Cryosphere, 8(4), 1317– 1329, https://doi.org/10.5194/tc-8-1317-2014.

Rounce, D. R., King, O., McCarthy, M., Shean, D. E., and Salerno, F. (2018). Quantifying debris thickness of debris-covered glaciers in the Everest region of Nepal through inversion of a subdebris melt model, J. Geophys. Res., 123(5), 1094– 1115, https://doi.org/10.1029/2017jf004395.

Rounce, D. R., Quincey, D. J., and McKinney, D. C. (2015). Debris-covered glacier energy balance model for Imja-Lhotse Shar Glacier in the Everest region of Nepal, The Cryosphere, 9(6), 2295– 2310, https://doi.org/10.5194/tc-9-2295-2015.

Rybak, O.O., Satylkanov, R., Rybak, E.A., Gubanov, A.S., Korneva, I.A., and Tanaka, K. (2021). Parameterization of Shortwave Solar Radiation in Glaciological Applications. Russ. Meteorol. Hydrol. 46, 495–506,. https://doi.org/10.3103/S106837392108001X.

Sakai, A., Fujita, K., and Kubota, J. (2004). Evaporation and percolation effect on melting at debris-covered Lirung Glacier, Nepal Himalayas, 1996, Bull. Glaciol. Res., 21, 9–15, 1592-1607.

Schaefli, B. and Huss, M. (2011). Integrating point glacier mass balance observations into hydrologic model identification, Hydrol. Earth Syst. Sci., 15, 1227–1241, https://doi.org/10.5194/hess-15-1227-2011.

Scherler, D., Wulf, H., and Gorelick, N. (2018). Global Assessment of Supraglacial Debris Cover Extents, Geophys. Res. Lett., 45, 11798–11805, https://doi.org/10.1029/2018GL080158.

Shaw, T. E., Brock, B. W., Fyffe, C. L., Pellicciotti, F., Rutter, N. and Diotri, F. (2016). Air temperature distribution and energy balance modelling of a debris-covered glacier, Journal of Glaciology, 1–14, https://doi.org/10.1017//jog.2016.31.

Shaw, T. E., Brock, B. W., Ayala, A., Rutter, N., and Pellicciotti, F. (2017). Centreline and cross-glacier air temperature variability on an Alpine glacier: assessing temperature distribution methods and their influence on melt model calculations, J. Glaciol., 6, 973–88, https://doi.org/10.1017/jog.2017.65.

Shaw, T.E., Ulloa, G., Farías-Barahona, D., Fernandez, R., Lattus, J.M., McPhee, J. (2021). Glacier albedo reduction and drought effects in the extratropical Andes, 1986-2020, J. Glaciol., 67(261), 158–169, https://doi.org/10.1017/jog.2020.102.

Smith, G. D. (1985). Numerical solutions of partial differential equations: finite difference methods, 3rd Edition, Oxford University Press, New York, 337 pp.

Steiner, J. F., Litt, M., Stigter, E. E., Shea, J., Bierkens, M. F. P., and Immerzeel, W. W. (2018). The importance of turbulent fluxes in the surface energy balance of a debris-covered glacier in the Himalayas, Front. Earth Sci., 6, 144, https://doi.org/10.3389/feart.2018.00144.

Steiner, J. F., Pellicciotti, F., Buri, P., Miles, E. S., Immerzeel, W. W., and Reid, T. D. (2016). Modelling ice-cliff backwasting on a debris-covered glacier in the Nepalese Himalaya, J. Glaciol., 61, 889–907, https://doi.org/10.3189/2015JoG14J194.

Stokes, C. R., Popovnin, V. V., Aleynikov, A. A., Gurney, S. D., and Shahgedanova, M. (2007). Recent glacier retreat in the Caucasus Mountains, Russia, and associated increase in supraglacial debris cover and supra-/proglacial lake development, Ann. Glaciol., 46, 195–203, https://doi.org/10.3189/172756407782871468.

Tielidze, L. G., Bolch, T., Wheate, R. D., Kutuzov, S. S., Lavrentiev, I. I., and Zemp, M. (2020). Supra-glacial debris cover changes in the Greater Caucasus from 1986 to 2014, The Cryosphere, 14, 585–598, https://doi.org/10.5194/tc-14-585-2020.

Van den Broeke, M. R. (1997). Momentum, heat, and moisture budgets of the katabatic wind layer over a midlatitude glacier in summer, J. Appl. Meteorol. Climatol., 36(6), 763-774, https://doi.org/10.1175/1520-0450(1997)036<0763:MHAMBO>2.0.CO;2.

Verhaegen, Y., Huybrechts, P., Rybak, O., and Popovnin, V. V. (2020). Modelling the evolution of Djankuat Glacier, North Caucasus, from 1752 until 2100 CE, The Cryosphere, 14, 4039–4061, https://doi.org/10.5194/tc-14-4039-2020.

Verhaegen, Y., Huybrechts, P., Rybak, O., and Popovnin, V. V. (subm.). Quantifying supraglacial debris-related melt-altering effects on the Djankuat Glacier, Russian Federation, Part 2: Using a modelling approach to derive the glacier-specific Østrem curve [in review].

Verhaegen, Y. and Huybrechts, P. (subm.). Model code for surface energy and mass balance modelling of clean ice and debris-covered ice on the Djankuat Glacier, Zenodo, https://doi.org/10.5281/zenodo.7451031.

Winter-Billington, A., Dadic, R., Moore, D., Flerchinger, G.N., Wagnon, P., and Banerjee, A. (2022). Modelling debris-covered glacier ablation using the Simultaneous Heat and Water transport model. Part 1: Model development and application to North Changri Nup, Frontiers in Earth Science, 10, Article 796877, https://doi.org/10.3389/feart.2022.796877.

WGMS (2022). Djankuat, North Caucasus, World Glacier Monitoring Service, available at: https://wgms.ch/products_ref_glaciers/djankuat/, last access: 17 November 2022.

Yang, W., Yao T., Zhu M., and Wang Y. (2017). Comparison of the meteorology and surface energy fluxes of debris-free and debris-covered glaciers in the southeastern Tibetan Plateau, J. Glaciol., 63(242), 1090-1104, https://doi.org/10.1017/jog.2017.77.